Comparative Analysis of Near-Storm Environmental Characteristics of Tornadoes in Northern and Southern China Based on Himawari-8 Satellite and ERA5 Data

Yang Zhao , Ruoxuan Li , Xiangzhen Kong * , Cheng Cheng , Yijian Chen , Kangkang Zhuang , Yinping Liu , Qilin Zhang

Posted Date: 10 April 2026

doi: 10.20944/preprints202604.0756.v1

Keywords: tornado; CAPE; wind shear; composite parameter

 doi:10.20944/preprints202604.0756.v1

Article

Comparative Analysis of Near-Storm Environmental Characteristics of Tornadoes in Northern and Southern China Based on Himawari-8 Satellite and ERA5 Data

Yang Zhao [1,2], Ruoxuan Li [2], Xiangzhen Kong [2,*], Cheng Cheng [2,3], Yijian Chen [2], Kangkang Zhuang [2], Yinping Liu [2] and Qilin Zhang [1,2]

[1] Collaborative Innovation Center on Forecast and Evaluation of Meteorological Disasters (CIC-FEMD) /State Key Laboratory of Climate System Prediction and Risk Management/Key Laboratory of Meteorological Disaster, Ministry of Education, Nanjing University of Information Science and Technology, Nanjing 210044, China

[2] School of Automation, Nanjing University of Information Science and Technology, Nanjing 210044, China

[3] Qujing Meteorological Bureau, 60 Qilin Lane, Qujing 655000, China

* Correspondence: kongxz@nuist.edu.cn

Highlights

What are the main findings?

- A clear regional difference exists in Chinese tornadogenesis. Southern tornadoes are "dynamically driven" in moist environments. Northern tornadoes follow a "coupled thermodynamic-kinematic" paradigm requiring substantial instability accumulation.
- Significant tornadoes (EF ≥ 2) exhibit distinct pre-storm vertical stretching signatures. These signatures are captured by rapid Himawari-8 satellite cloud-top cooling (TBB ≤ -73 °C).

What are the implications of the main findings?

- Combining high-frequency geostationary satellite observations with atmospheric reanalysis mitigates ground-radar blind spots. This approach provides a method for continuously monitoring pre-tornadic severe convective storms.
- The temporal intensification of environmental indices provides reliable, quantitative precursor signals for short-term nowcasting. This highlights the need to regionally recalibrate operational tornado warning thresholds in China.

Abstract

Continuous monitoring and nowcasting of tornadic near-storm environments remain challenging, particularly in regions with limited ground-based weather radar coverage. High-spatiotemporal-resolution geostationary satellite remote sensing offers a valuable approach to track the evolution of severe convective storms. Combining 10-minute cloud-top brightness temperature (TBB) data from the Himawari-8 satellite and ERA5 reanalysis, this study investigates the atmospheric environments of 177 documented tornadoes in China from 2016 to 2023. Tracking storm convective centers using TBB minima reveals clear regional differences in tornadogenesis paradigms. Southern China tornadoes exhibit a "dynamically driven" pattern within quasi-steady, warm, and moist environments. These environments feature low Lifted Condensation Levels (LCL; ~790 m) and weak Convective Inhibition (CIN). Intense low-level wind shear and storm-relative helicity (SRH) dominate the convective triggering. Northern China tornadoes follow a "coupled thermodynamic-kinematic" paradigm under relatively drier and cooler backgrounds. Their initiation relies on the rapid, synchronized accumulation of Mixed-Layer convective available potential energy (MLCAPE) and deep-layer SRH. Furthermore, intensity-based comparative analysis indicates that significant tornadoes (Enhanced Fujita [EF] scale, EF ≥ 2) are favored by higher MLCAPE, deep-layer shear, and

 doi:10.20944/preprints202604.0756.v1

lower LCLs compared to weak ones (EF ≤ 1). Himawari-8 TBB data capture a more rapid pre-storm convective cloud-top cooling for strong tornadoes, with medians reaching -73 °C. This study demonstrates that combining high-frequency satellite observations with reanalysis data provides quantitative precursor signals for regional severe tornado nowcasting.

Keywords: tornado; CAPE; wind shear; composite parameter

1. Introduction

Approximately 100 tornadoes occur in China annually [1]. Although this frequency is substantially lower than that in the United States, the associated societal impacts and casualties are often disproportionately severe. For instance, on 4 October 2015, two tornadoes spawned by Typhoon Mujigae in Foshan and Guangzhou, Guangdong Province, claimed 7 lives and injured 229 people [2]. Similarly, a violent tornado at Suzhou, Jiangsu Province, on 14 May 2021 resulted in 4 fatalities and 151 injuries [3]. This high vulnerability is primarily due to tornadogenesis in China occurring heavily in the eastern regions. These areas coincide with the nation's highest population density and most intensive economic activities. Another critical factor is the current inadequacy in operational tornado monitoring capabilities and our limited understanding of their behavioral characteristics. Eastern China spans over 40 degrees of latitude from south to north, encompassing diverse climatic zones that yield pronounced regional variations in tornadic behaviors[4]. This spatial heterogeneity poses challenges to operational tornado nowcasting and warning, highlighting the need to investigate regional tornadogenesis patterns and their favorable atmospheric environments across China.

Previous studies have shown that tornadogenesis is closely linked to a combination of thermodynamic and kinematic environmental parameters [5–9]; nevertheless, these relationships exhibit remarkable regional dependencies. Typically, elevated Convective Available Potential Energy (CAPE), lower Lifted Condensation Levels (LCL), and intense vertical wind shear (SH) constitute the primary environmental prerequisites for tornadic storms. Strong SH is vital for the organization and longevity of severe thunderstorms, while considerable storm-relative helicity (SRH) plays a pivotal role in the generation of low-level mesocyclones and subsequent tornadogenesis [10–14]. Satellite-observed cloud-top brightness temperature (TBB) serves as a critical proxy for diagnosing the depth and vigor of convective updrafts, bridging ambient macroscale instability with the internal physical processes of the storm. Composite parameters that integrate both thermodynamic and kinematic ingredients include the Energy-Helicity Index (EHI), Supercell Composite Parameter (SCP), and Significant Tornado Parameter (STP). EHI exceeding 2.0 or an STP greater than 1.0 is generally regarded as a conducive environmental threshold for significant tornadoes [8,15,16].

On a global scale, tornadic near-storm environments exhibit pronounced regional disparities. In the United States, the central Great Plains typically feature classical severe convective environments characterized by large CAPE and strong deep-layer shear, whereas the southeastern U.S. is frequently dominated by "high-shear, low-CAPE" (HSLC) regimes [17]. Additionally, compared to European tornadic environments, those in the U.S. generally possess richer boundary-layer moisture and greater Convective Inhibition (CIN). This stronger capping inversion makes convective initiation more difficult, but facilitates much more rapid updraft development once triggered [18].

Existing literature indicates that tornadic environments in China also exhibit distinct geographical differences [19]. Southern China tornadoes typically present a "dynamically-driven" paradigm (frequently associated with tropical cyclones and the Meiyu front). They are characterized by strong low-level wind shear and helicity, alongside relatively modest CAPE and low LCLs [20,21]. Conversely, northern China tornadoes follow a "strong-thermodynamic, weak-kinematic" regime. Their initiation relies on abundant CAPE, while the magnitude of low-level wind shear is weaker than that of their southern counterparts [22,23]. However, previous studies have largely been confined to individual case studies or statistical analyses of specific synoptic weather systems. There remains an obvious lack of systematic comparative investigations into the environmental differences

 doi:10.20944/preprints202604.0756.v1

between northern and southern China. In particular, comparative analyses incorporating high-resolution satellite observations of pre-storm cloud-top signatures are virtually non-existent.

To date, systematic observational datasets for Chinese tornadoes remain inadequate. Most prior climatological efforts have relied on textual archives, such as meteorological yearbooks, which occasionally suffer from inherent spatiotemporal ambiguities. The sparse coverage of operational ground-based Doppler weather radars in certain regions poses significant challenges in pinpointing the tornadic parent storms. To overcome these observational limitations, high-spatiotemporal-resolution geostationary satellites (e.g., Himawari-8) offer an indispensable tool for continuously monitoring cloud-top evolution. Consequently, by utilizing Himawari-8 satellite observations and ERA5 reanalysis data, this study tracks the pre-storm convective centers of a filtered dataset of well-documented tornado events. By examining the temporal evolution of near-storm environmental parameters during the three hours preceding tornadogenesis, this study aims to investigate the regional differences in tornadic environments across China and explore their underlying physical mechanisms.

2. Data and Method

2.1. Tornado Event Data

The tornado event data utilized in this study are derived from published annual climatological reports of tornado disasters in China [3,24–29]. We incorporated events labeled as "confirmed" with solid evidentiary support from the Tornado Database in China (2017–2020), which is publicly archived on the Peking University Open Research Data Platform [30]. To ensure maximum data fidelity, these preliminary tornado records were further cross-verified against official reports from local meteorological departments and the Key Laboratory for Tornadoes, China Meteorological Administration (CMA). This rigorous screening process yielded a comprehensive dataset comprising 189 well-documented tornado events with precise occurrence times and geographical coordinates (Figure 1).

To guarantee the robustness of the subsequent near-storm environmental analyses, rigorous quality control was performed to assess the reliability and completeness of both the Himawari-8 TBB observations and the ERA5 reanalysis fields for each individual event. Initially, events exhibiting anomalously warm minimum TBB values (warmer than -30 °C) were excluded, as strong deep convective activity typically warrants a colder TBB threshold [31]. Subsequently, an additional 10 events were discarded due to anomalously low CAPE values (less than10 J kg^{-1}) coupled with missing CIN records. All these excluded events associated with anomalous gridded data were situated in northern China. The ensuing analyses focus on the refined cohort of the remaining 177 high-quality tornado events. The Qinling-Huaihe Line is the recognized geographical and climatic boundary between northern and southern China. Based on this boundary, the tornadoes were stratified into a Southern China group (S. China) and a Northern China group (N. China).

 doi:10.20944/preprints202604.0756.v1

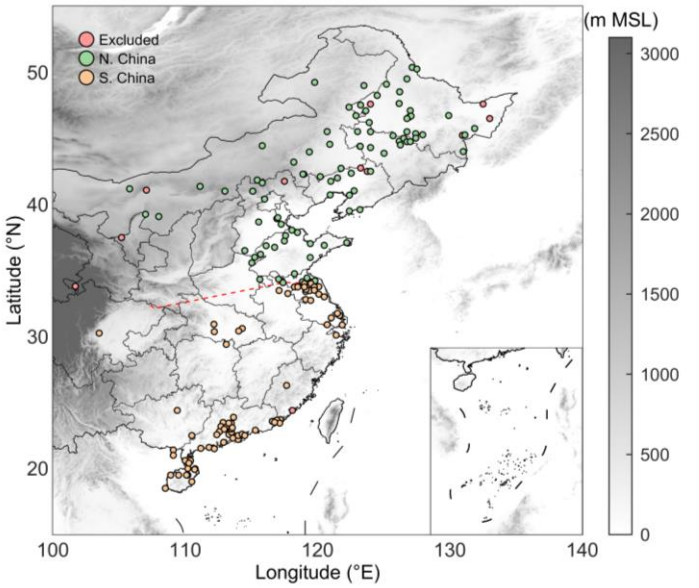

Figure 1. Spatial distribution of 189 documented tornado events in China from 2016 to 2023. The red dashed line denotes the Qinling-Huaihe Line, which acts as the geographical dividing line between northern and southern China. Shading represents terrain elevation (m MSL).

Among the 177 retained tornado events, 94 were assigned an Enhanced Fujita (EF) scale rating, comprising 10 EF0, 37 EF1, 28 EF2, 16 EF3, and 3 EF4 tornadoes. Given the relatively limited sample sizes across individual intensity sub-categories, we aggregated the dataset based on established EF-scale characteristics [32]. The 47 tornadoes rated EF0 and EF1 were classified as weak tornadoes (EF ≤ 1), while the remaining 47 events rated EF2 or higher were categorized as significant tornadoes (EF ≥ 2). Table 1 details the intensity distribution within the two regional subsets. It is evident that the proportion of significant tornadoes (EF ≥ 2) in northern China (59%) is higher than that observed in southern China (42%). This finding aligns with Zhang et al. [33], whose climatological analysis of 129 significant tornadoes revealed that central China experiences the highest frequency of such intense events (accounting for 62%). The underlying physical mechanisms driving this regional disproportion in tornado intensity will be explored in subsequent sections.

Table 1. Distribution of EF ratings for 177 tornado events.

Region	N	EF ≤ 1	EF ≥ 2	Unclassified
Southern China	86	29	21	36
Northern China	91	18	26	47
Total	177	47	47	83

2.2. Atmospheric Environmental Parameters

TBB data utilized in this study were derived from Band 14 (11.24 μm) of the Himawari-8 geostationary satellite [34], featuring a spatial resolution of 0.1° × 0.1° and a temporal interval of 10 min. Relevant thermodynamic, kinematic, and composite environmental parameters were calculated based on the ERA5 reanalysis dataset [35], utilizing temperature, humidity, wind, and pressure data across 20 pressure levels spanning from 1000 to 100 hPa. The ERA5 data possess a spatial resolution of 0.25° × 0.25° and an hourly temporal resolution.

SRH within the 0–1 km (SRH1), 0–3 km (SRH3), and 0–6 km (SRH6) layers was computed following the definitions provided by Markowski and Richardson [36]. The mixed-layer lifted condensation level (MLLCL) was calculated utilizing the exact analytical expression proposed by

 doi:10.20944/preprints202604.0756.v1

Romps [37]. It is worth noting that the magnitudes of CAPE and CIN are highly sensitive to the choice of the initial lifted parcel (e.g., surface-based, mixed-layer, and most-unstable parcels). We calculated and compared these three variants of CAPE and CIN (Figure A1 and A2). The mixed-layer parameters (MLCAPE and MLCIN) were selected as the primary metrics to represent atmospheric instability and convective inhibition in the ensuing analyses. The composite parameters, including STP, EHI, and SCP, were derived adhering to the formulations established by Thompson et al. [8].

2.3. Identification of Tornadic Convective Centers

In this study, the analysis of near-storm environmental parameters was specifically targeted at the grid point (0.25° × 0.25°) corresponding to the intense convective core of the tornadic parent storm. While ground-based weather radar observations are the ideal proxy for identifying convective centers, ensuring uniform radar coverage for the large and widely distributed tornado events analyzed in this study is computationally and logistically challenging. As this research focuses on the statistical relationship between tornadogenesis and macro-environmental parameters, rather than investigating cloud microphysics or internal storm dynamics, radar data were bypassed. Instead, Himawari-8 TBB data were employed to determine the locations of the convective centers [38].

The tracking methodology proceeded as follows: First, a 2° × 2° spatial domain was established, centered on the exact geographical coordinates of the tornado occurrence. Subsequently, the specific grid point exhibiting the absolute minimum TBB value within this predefined domain was retrieved. This grid point was then designated as the environmental sampling location at the time of tornadogenesis (denoted as 0 h, approximated to the nearest synoptic hour relative to the actual tornado occurrence).

Given that the lifecycles of the tornado-producing convective systems in this study fall within a 3-hour window, we analyzed the environmental parameters during the three hours preceding tornadogenesis (-1 h, -2 h, and -3 h). We identified the intense convective centers during the preceding three hours by tracking backward from their 0 h positions. This tracking was guided by the storm's motion direction and translation speed derived from consecutive satellite imagery. A detailed step-by-step illustration of this tracking methodology for a representative tornado case is provided in Figure A3.

3. Results

Low-level atmospheric boundary layer moisture serves as one of the critical precursor parameters for assessing tornadogenesis potential, as it modulates the available buoyant energy and moisture supply requisite for convective development. Generally, near-surface humidity in southern China is higher than that in the north. This climatological disparity likely leads to pronounced regional differences in both tornadic environmental characteristics and ultimate tornado intensities. To investigate these disparities, the ensuing sections will analyze the atmospheric environmental variables, stratifying the dataset by region (northern vs. southern China) and by tornado intensity.

Extensive prior studies have demonstrated that LCL, CAPE, CIN, alongside SRH and SH, constitute the primary environmental ingredients modulating tornadic activity. Consequently, the following analyses will focus on these fundamental parameters and the composite indices derived from their synthesis.

3.1. Comparative Analysis of Near-Storm Environmental Parameters between Northern and Southern China

3.1.1. Thermodynamic Parameters

LCL reflects the low-level atmospheric moisture content. Figure 2a illustrates the temporal evolution of the MLLCL at the time of tornadogenesis (0 h) and during the three preceding hours. It is evident that the MLLCLs associated with southern tornadoes are lower than those in the north, with these regional differences achieving statistical significance across all four time steps based on

 doi:10.20944/preprints202604.0756.v1

the Mann-Whitney U test. The southern MLLCLs are highly concentrated, whereas the northern MLLCLs exhibit a broader spread. During the three hours leading up to tornadogenesis, the estimated cloud-base heights (represented by MLLCL) for both regional groups remain largely quasi-steady (Friedman analysis of variance, $p > 0.05$). This temporal stationarity suggests that MLLCL functions primarily as a background environmental precondition rather than a rapidly evolving, short-term nowcasting precursor for tornadogenesis.

Satellite-derived TBB characterizes cloud-top height and convective intensity; colder TBB values denote higher cloud tops and more vigorous convective updrafts. As depicted in Figure 2b, the near-storm TBBs for southern tornadoes are colder than those in the north across all tracked times (e.g., at 0 h, the median TBB is -75 °C for the south versus -54 °C for the north). This implies that the parent thunderstorms of southern tornadoes feature higher cloud tops and stronger convective intensity than their northern counterparts, a finding consistent with previous climatological studies on thunderstorms across China [39].

From a temporal perspective (from -3 h to 0 h), the TBBs of the tornadic parent storms in both regions exhibit a significant cooling trend (Friedman test, $p < 0.001$). This trajectory captures the continuous vertical lifting of the cloud tops and the progressive intensification of convective activity leading up to tornadogenesis. The evolutionary characteristics of MLLCL and TBB (Figure 2) reveal a clear kinematic-thermodynamic signature: while the LCLs in both regions remain largely invariant during the three pre-tornadic hours, the corresponding TBBs undergo continuous cooling. The median TBB for southern tornadic storms drops by 11 °C over this three-hour window, compared to an 8 °C decrease observed in northern storms. This steeper cooling gradient demonstrates that the vertical stretching and deep-layer development of the parent thunderstorm clouds are more vigorous in southern China than in the north.

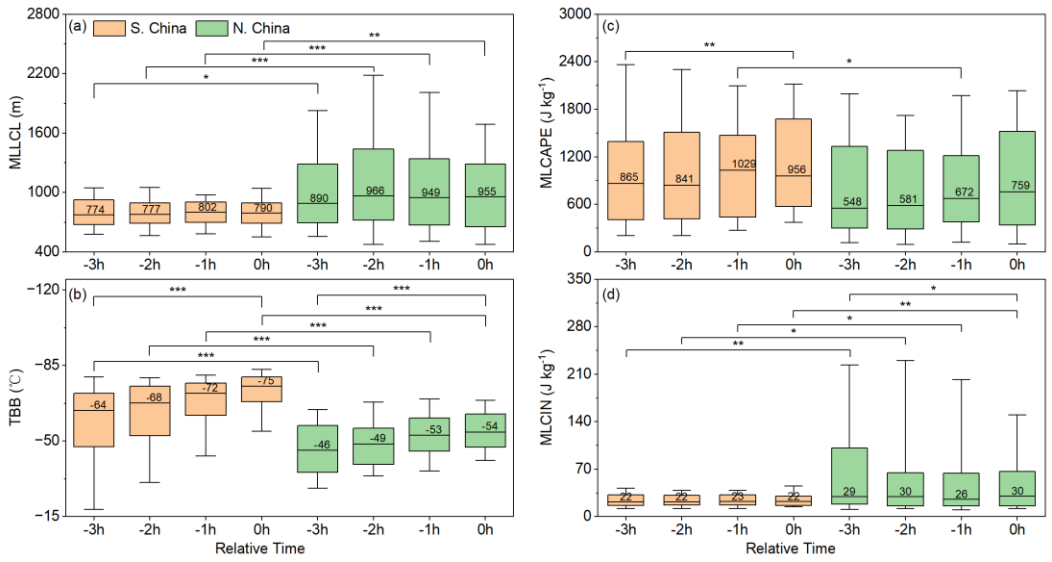

Figure 2. Temporal evolution of thermodynamic parameters at convective centers for 177 tornadoes: (a) MLLCL, (b) TBB, (c) MLCAPE, and (d) MLCIN. Numbers embedded within the boxes indicate the median values. Short horizontal lines with asterisks denote the statistical significance of differences between the Southern and Northern China groups at the same relative time (Mann-Whitney U test). Long overarching lines denote the significance of the temporal evolutionary trend within each region (Friedman test; * $p < 0.05$, ** $p < 0.01$, *** $p < 0.001$).

CAPE and CIN serve as two core thermodynamic parameters for assessing atmospheric convective potential and initiation conditions. As illustrated in Figure 2c, the near-storm environments of southern tornadoes generally possess higher overall MLCAPE values. Temporally,

 doi:10.20944/preprints202604.0756.v1

MLCAPE in both regions exhibits an increasing trend prior to tornadogenesis. However, while this accumulation is relatively modest for southern tornadoes, northern tornadoes undergo a significant pre-storm amplification, with the median MLCAPE increasing rapidly from 548 J kg^{-1} to 759 J kg^{-1}. This contrast suggests that abundant CAPE is likely a common background condition in southern tornadic environments, rather than a primary limiting factor for tornadogenesis. In the north, the rapid accumulation of instability (i.e., the pronounced pre-storm spike in MLCAPE) appears much more critical. This aligns with the characteristics of tornadoes in Liaoning Province, which require substantial buoyant energy to compensate for their relatively low-humidity ambient environments [23]. In the moisture-starved northern regions, this imminent, rapid buildup of instability may serve as a decisive factor dictating whether a tornado will spawn.

On the other hand, the median CIN values for both regions are relatively small and remain temporally quasi-steady (Figure 2d). The median MLCIN for southern tornadoes consistently hovers at a low magnitude of approximately 22 J kg^{-1}, whereas the northern MLCIN is higher. This regional divergence corroborates previous localized studies noting minimal CIN in the environments of tropical cyclone (TC) tornadoes in Guangdong [20] and relatively higher CIN for tornadoes in Liaoning [22]. Overall, compared to the south, northern tornadic environments are characterized by relatively lower boundary-layer humidity, higher CIN, and a pronounced pre-storm amplification of CAPE. The comparatively higher CIN in the north acts as an effective "capping inversion" (or "energy lid"), suppressing the premature release of early, weak convection. This suppression affords the boundary layer ample time to accumulate instability until it reaches a magnitude sufficient to trigger deep, violent convection [18]. Thermodynamically, this mechanism likely constitutes a crucial explanation for the higher proportion of significant tornadoes (EF ≥ 2) observed in northern China relative to the south.

3.1.2. Kinematic Parameters

Figure 3a illustrates the storm-relative helicity integrated from the surface to 1 km, 3 km, and 6 km AGL (denoted as SRH1, SRH3, and SRH6) at the convective centers of the 177 tornadoes across different tracking times. Overall, the median SRH values for southern tornadoes in the low-to-mid levels (SRH1 and SRH3) generally exceed those in the north, although this regional difference achieves statistical significance within the lowest layer (SRH1). This regional gap narrows in the deep layer (SRH6). At the time of tornadogenesis (0 h), the median SRH6 for northern tornadoes (124 m^2 s^{-2}) even slightly surpasses its southern counterpart (122 m^2 s^{-2}).

Regarding temporal evolution, the northern SRH1 exhibits a statistically significant progressive intensification leading up to 0 h, whereas southern tornadoes experience a pronounced enhancement in SRH3. These evolutionary trajectories suggest that low-to-mid-level SRH serves as the primary kinematic driver for tornadogenesis. While SRH magnitude increases with height in both regions, the vertical gradient is steeper in the north. For instance, at 0 h, the median difference between SRH6 and SRH1 in the north reaches a remarkable 84 m^2 s^{-2}, whereas the corresponding vertical increment in the south is 47 m^2 s^{-2}.

 doi:10.20944/preprints202604.0756.v1

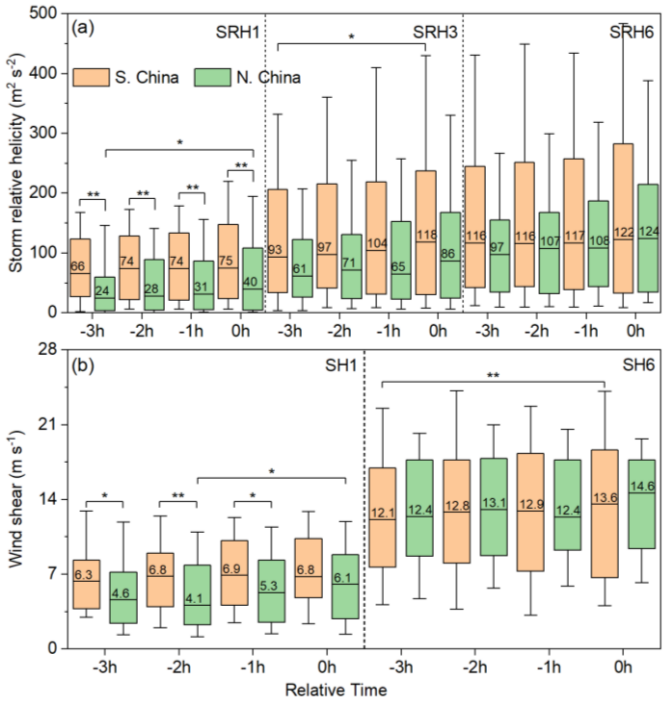

Figure 3. As in Figure 2, but for kinematic parameters: (a) storm-relative helicity and (b) vertical wind shear.

SH across different altitude layers impacts storm structure and rotational characteristics. Low-level SH (0–1 km, hereafter SH1) serves as the primary source of the intense near-ground rotation required for tornadogenesis [16,40]. Deep-layer SH (0–6 km, hereafter SH6) maintains the mesocyclone by dynamically separating the updraft and downdraft, thereby organizing the storm into a "supercell" mode [8]. Figure 3b displays the temporal distributions of SH1 and SH6 for northern and southern tornadoes. Generally, the ambient SH1 in the south is higher than that in the north. While the median SH6 values for both regions are comparable, the northern SH6 exhibits a significant, sustained intensifying trend prior to tornadogenesis (Friedman test, $p < 0.01$).

Combining these SH characteristics with the preceding SRH analysis reveals that the strong SH1 in southern environments aligns with their intense SRH1. This consistency suggests that their strongly rotating convective structures are predominantly governed by low-level SH. Superimposed upon the moist boundary layer in the south, this tight coupling of "strong low-level kinematics and high-humidity, warm thermodynamics" amplifies the probability of tornadogenesis. Although the northern SH1 is comparatively weaker, these environments possess deep-layer kinematic conditions (evidenced by strong SH6 and prominently surpassing SRH6) that rival or even exceed those in the south. This implies that the generation of systemic helicity in northern storms relies on the "compensatory" forcing of deep-layer SH, predisposing the initial storm rotation to originate preferentially in the mid-to-upper levels.

3.1.3. Composite Parameters

Although a statistical assessment of individual thermodynamic and kinematic variables has revealed distinct regional contrasts in tornadic environments, tornadogenesis arises from the forcing of multiple coexisting conditions. This study further investigates the composite parameters: EHI, SCP, and STP. Figure 4a and 4b presents the temporal evolution of EHI1 and EHI3, computed based on SRH1 and SRH3, respectively. The northern region (N. China) shows a distinct "kinematically-driven" signature, with its EHI1 and EHI3 undergoing significant ($p < 0.01$) and highly significant ($p < 0.001$) continuous amplification immediately prior to tornadogenesis. This trajectory delineates the rapid establishment of low-to-mid-level storm rotational potential.

 doi:10.20944/preprints202604.0756.v1

Operationally, an SCP value exceeding 1.0 is generally considered highly conducive to intense supercell development [8]. As observed in Figure 4c, the median SCP for northern parent thunderstorms maintains a relatively subdued baseline initially but registers a prominent pre-storm surge. The SCP in the southern region (S. China) exhibits minimal temporal variability, consistently maintaining values near 1.0. This stable temporal trend suggests that southern tornadoes spawn within a quasi-steady, favorable environment. Their initiation is likely governed by mesoscale triggers rather than sudden synoptic-scale changes.

As illustrated in Figure 4d, within the two hours leading up to tornadogenesis, the median STPs for both regional environments exhibit an ascending trajectory. This widespread, significant pre-storm enhancement of STP ($p < 0.05$) underscores its operational efficacy as an integrated metric for short-term tornado nowcasting. At the exact time of tornadogenesis (0 h), the northern median STP (0.60) is higher than the southern median (0.48), providing further environmental-potential justification for the relatively higher proportion of significant tornadoes in northern China. It is noteworthy that the median STPs for both regions (~0.5) fall below the classical warning thresholds operationally established in the United States. This notable discrepancy highlights the need to recalibrate operational warning criteria to accommodate the unique regional climatological characteristics native to China.

Overall, for the northern region, all four evaluated composite parameters exhibit clear increasing trends within the two hours preceding tornadogenesis. For the southern region, however, only EHI3 and STP exhibit such prominent short-term amplifications. This demonstrates that the abrupt short-term spikes (i.e., steepening slopes) of the EHI and STP indices function as valuable precursor signals for operational tornado nowcasting across China.

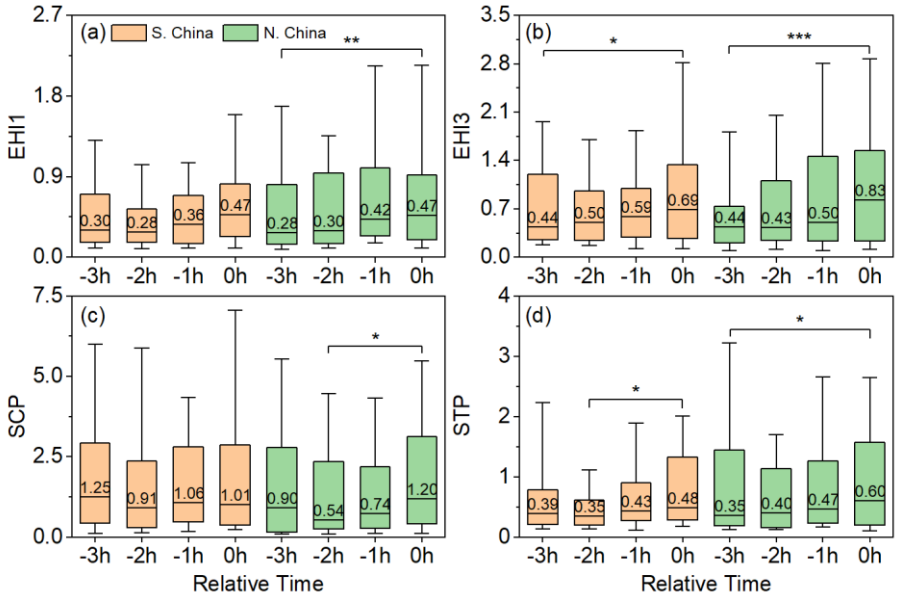

Figure 4. As in Figure 2, but for composite parameters: (a) EHI1, (b) EHI3, (c) SCP, and (d) STP.

To better visualize the systematic disparities in environmental parameter configurations between northern and southern tornadoes, we further evaluated the bivariate kernel density estimation (KDE) distributions of key thermodynamic and kinematic variables (Figure 5). As illustrated in Figure 5a, the pre-tornadic environments of the two regions exhibit a pronounced separation within the parameter phase space. The distribution centroid for southern tornadoes (orange contours) is concentrated in the regime characterized by elevated MLCAPE and strong SH1. This configuration corroborates their inherent reliance on the favorable coupling of thermodynamics and low-level kinematics within a warm and moist background. The core density region for northern tornadoes (green contours) is clustered in the lower-left quadrant, signifying environments characterized by relatively diminished instability and weaker SH1.

 doi:10.20944/preprints202604.0756.v1

Given that northern environments lack a definitive advantage in both low-level thermodynamics and kinematics, what mechanism triggers their significant tornadoes? Figure 5b yields a critical clue: Although SRH6 and SH1 exhibit an overall positive correlation in both regions, under weak low-level shear conditions, the green contours representing northern environments exhibit a steeper ascending trajectory, indicating a higher ratio of SRH6 to SH1 under weak low-level shear conditions. This distinct signature dictates that northern tornadogenesis is frequently accompanied by—and reliant upon—strong deep-layer kinematic support (SRH6) to function as a "compensatory" forcing mechanism. This phase-space evidence forms a consistent physical interpretation with the preceding analytical deduction that northern environments possess superior deep-layer kinematic potential.

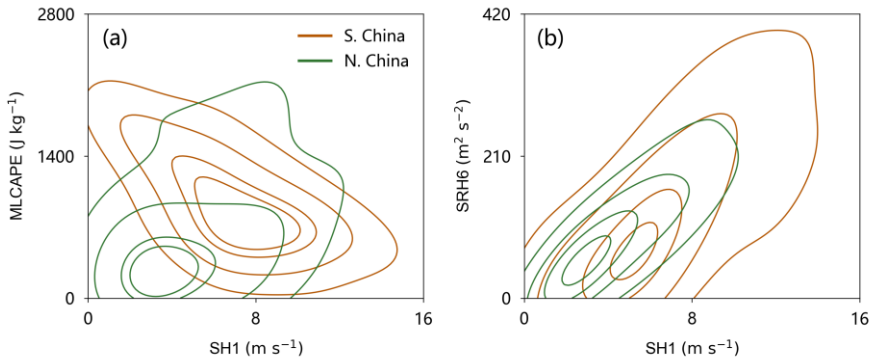

Figure 5. Bivariate kernel density estimation (KDE) plots illustrating the environmental parameter phase space at the time of tornadogenesis (0h): (a) MLCAPE versus SH1, and (b) SRH6 versus SH1. The contours from the outermost to innermost represent the 90th, 75th, 50th, and 25th percentiles of the KDE values, respectively.

Based on the systematic analyses of the individual and composite parameters delineated above, the tornadic near-storm environments across northern and southern China can be conceptualized into two divergent physical paradigms:

The southern tornadic environment constitutes a classical "dynamically-driven" paradigm. These tornadoes are formed within a warm, moist, and "quasi-steady" background characterized by abundant low-level moisture and minimal CIN. Their initiation and subsequent evolution are driven by potent low-level kinematic ingredients (specifically, strong SH1 and SRH1).

In contrast, the northern tornadic environment represents a "coupled thermodynamic-kinematic" paradigm. Under an adverse, comparatively cooler and drier ambient background featuring substantial initial CIN (which acts as an effective lid for energy accumulation), disorganized, weak convective attempts are filtered out. The outbreak of significant tornadoes in this regime relies on a surge in thermodynamic instability, indicated by the pre-storm amplification of MLCAPE. It also requires concurrent kinematic compensation from stronger deep-layer kinematics (specifically, intense SH6 and SRH6). Only through this concurrent amplification of thermodynamic and kinematic factors can the parent storm overcome the initial environmental capping inversion, triggering a significant tornado characterized by a deep rotational structure.

To further explore the synoptic-scale physical mechanisms underlying the regional disparities in tornadic environmental parameters across China, a composite analysis of the large-scale circulation fields at 500 hPa and 850 hPa at the time of tornadogenesis (0 h) was conducted utilizing ERA5 reanalysis data (Figure 6). The results indicate that northern and southern tornadoes are governed by distinct synoptic weather systems, thereby providing a macroscopic physical explanation for their divergent near-storm environmental signatures.

For northern tornadoes, the tornadogenesis region in the mid-to-upper troposphere at 500 hPa (Figure 6a) is steered by a deep cold trough or the Northeast Cold Vortex (NECV) system, manifesting as a prominent geopotential height minimum accompanied by intense northwesterly or westerly cold advection. In the lower troposphere at 850 hPa (Figure 6c), a distinct closed cyclonic vortex is evident.

 doi:10.20944/preprints202604.0756.v1

This "upper-level cold trough coupled with a low-level cyclone" synoptic configuration advects dry, cold air aloft over the relatively warm and moist air near the surface, steepening the atmospheric vertical lapse rate. This dynamically forced steepening well explains why, despite prevailing in an environment with relatively limited near-surface moisture (i.e., higher MLLCLs), the northern MLCAPE can undergo rapid pre-storm accumulation and amplification (Figure 2c). Concurrently, this deep low-pressure system imparts intense systemic kinematic forcing to the mid-to-upper levels, substantiating that northern tornadoes are dependent on strong SH6, SRH3, and SRH6. The "coupled thermodynamic-kinematic " paradigm mechanism governing northern tornadogenesis is essentially the integrated product of severe stratification instability and deep-layer kinematic shear concurrently driven by the deep cold vortex system.

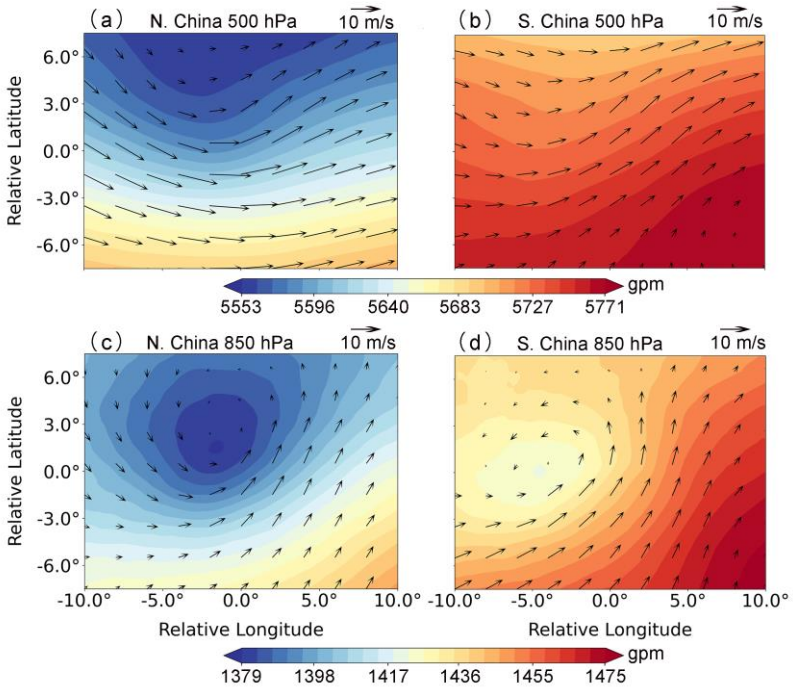

Figure 6. Composite large-scale environmental fields at the time of tornadogenesis (0h). (a) 500 hPa and (c) 850 hPa for Northern China; (b) 500 hPa and (d) 850 hPa for Southern China. Shading represents geopotential height (gpm), and arrows denote horizontal wind vectors (m s^{-1}).

The synoptic-scale circulation background for southern tornadoes exhibits pronounced disparities. At 500 hPa (Figure 6b), the southern region is primarily situated along the periphery of the western North Pacific subtropical high (WNPSH). The geopotential height field here is generally elevated and relatively flat, dominated by a quasi-zonal southwesterly flow. However, at 850 hPa (Figure 6d), the tornadogenesis region is dictated by a strong southwesterly low-level jet (LLJ). This strong LLJ transports abundant warm, moist maritime air from the tropical oceans inland, creating a typical thermodynamic profile of southern tornadic environments: abundant boundary-layer moisture, low MLLCLs, and minimal MLCIN. The intense low-level wind speed maximum generates SH1 and SRH1 within the boundary layer. From a synoptic-dynamic perspective, this circulation configuration provides a clear physical basis for the "dynamically-driven" nature of southern tornadoes: within a high-temperature, high-humidity, quasi-steady environment, the vigorous LLJ operates as the definitive kinematic trigger for tornadogenesis.

 doi:10.20944/preprints202604.0756.v1

3.2. Comparative Analysis of Near-Storm Environmental Parameters between Significant and Weak Tornadoes

While the preceding analyses have identified the typical features and regional differences in tornadic near-storm environments across China, these large-scale spatial patterns do not capture the inherent relationships between environmental conditions and the resulting tornado intensity. The dataset is subsequently re-stratified based on EF scale ratings to investigate the evolutionary disparities in pre-storm environmental characteristics. Focusing on a subset of 94 well-documented tornado events with explicit EF ratings, this section explores the pre-storm features of key thermodynamic, kinematic, and composite parameters for weak tornadoes (EF ≤ 1) versus significant tornadoes (EF ≥ 2).

Figure 7 illustrates the temporal evolution of key thermodynamic parameters, MLLCL and TBB, prior to tornadogenesis for both intensity groups. As depicted in Figure 7a, at the exact time of tornadogenesis (0 h), the median MLLCL for significant tornadoes (748 m) is lower than that for weak tornadoes (867 m). This substantial disparity indicates that the initiation of significant tornadoes is predisposed to environments featuring more abundant near-surface boundary-layer moisture and correspondingly lower cloud bases.

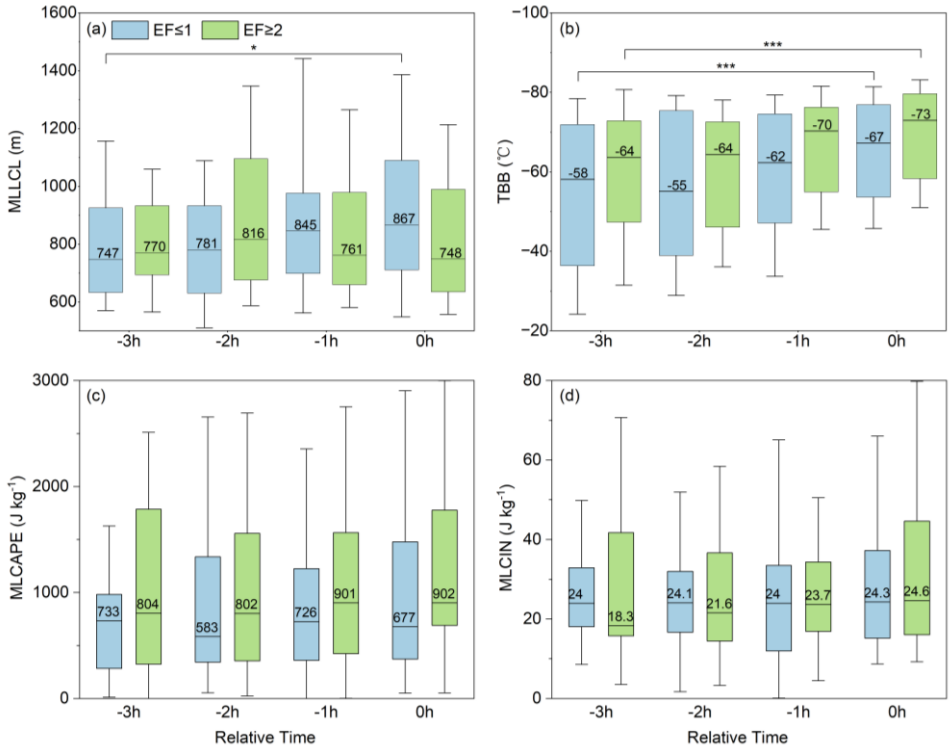

Figure 7. Temporal evolution of thermodynamic parameters for 94 tornadoes with clear EF ratings: (a) MLLCL, (b) TBB, (c) MLCAPE, and (d) MLCIN. Numbers embedded within the boxes indicate the median values. Short horizontal lines with asterisks denote the statistical significance of differences between the weak (EF ≤ 1) and significant (EF ≥ 2) tornado groups (Mann-Whitney U test). Long overarching lines denote the significance of the temporal evolutionary trend within each intensity group (Friedman test; *$p < 0.05$, **$p < 0.01$, ***$p < 0.001$).

The temporal evolution of MLLCL exhibits divergent trends between the weak and significant tornadic environments leading up to initiation. During the three hours preceding tornadogenesis, the MLLCL for weak tornadoes shows a statistically significant, sustained ascending trend (i.e., progressive boundary-layer drying; Friedman test, $p < 0.05$), with the median elevating from 747 m to 867 m. The MLLCL for significant tornadoes undergoes a distinct decrease within the final two hours prior to genesis (median decreasing from 816 m to 748 m), reflecting a pronounced near-surface moistening process. Unlike the pure regional stratification (Figure 2), which yielded no significant

 doi:10.20944/preprints202604.0756.v1

temporal trends in MLLCL, stratifying by tornado intensity reveals a clear divergence. This ascending versus descending trend in pre-storm MLLCL is closely tied to the ultimate tornado intensity. Therefore, this divergent boundary-layer evolutionary behavior serves as a vital environmental precursor signal for discriminating the potential of significant versus weak tornadogenesis.

As illustrated in Figure 7b, the median TBB for significant tornadic environments (-73 °C) is colder than that for weak tornadoes (-67 °C), indicating that the parent thunderstorms of significant tornadoes typically possess higher cloud tops. Regarding temporal evolution, the TBBs for both intensity groups exhibit a significant cooling trend prior to tornadogenesis, commencing at -2 h (Friedman test, $p < 0.001$). The median TBB for weak tornadoes decreases from -55 °C to -67 °C, whereas the median for significant tornadoes decreases rapidly from -64 °C to -73 °C. This steeper cooling gradient reflects the continuous lofting of cloud tops and the vigorous intensification of convective updrafts. For significant tornadoes, a decreasing MLLCL (lowering cloud base) coincides with a rapidly dropping TBB (ascending cloud top). These simultaneous changes indicate strong vertical stretching of the parent storm immediately before tornadogenesis.

Figure 7c reveals that at the exact time of tornadogenesis (0 h), the median MLCAPE for significant tornadoes (902 J kg^{-1}) is higher than that for weak tornadoes (677 J kg^{-1}). This disparity suggests a positive correlation between the ultimate tornado intensity and the reservoir of instability harbored within the near-storm environment. Temporally, the median MLCAPE for weak tornadoes fluctuates during the three pre-storm hours, lacking a discernible amplifying trend (even experiencing a marginal decrease from 733 J kg^{-1} at -3 h to 677 J kg^{-1} at 0 h). On the other hand, the accumulation of instability for significant tornadoes is far more pronounced; the median MLCAPE achieves a steady, progressive surge (increasing from 802 J kg^{-1} at -2 h to 902 J kg^{-1} at 0 h) within the final two hours preceding genesis. MLCIN exhibits no statistically significant discrepancy between the significant and weak tornadic environments; both groups maintain low and comparable magnitudes (Figure 7d). This indicates that minimal MLCIN is likely a favorable background precondition for general tornadogenesis; however, its absolute magnitude is insufficient to discriminate the ultimate intensity of the ensuing tornado. The pronounced pre-storm descent in MLLCL, coupled with the rapid decrease in TBB (reaching -73°C), clearly illustrates the strong vertical stretching of the parent storm. This process is characterized by a rapidly descending, moistening cloud base synchronized with an ascending cloud top.

 doi:10.20944/preprints202604.0756.v1

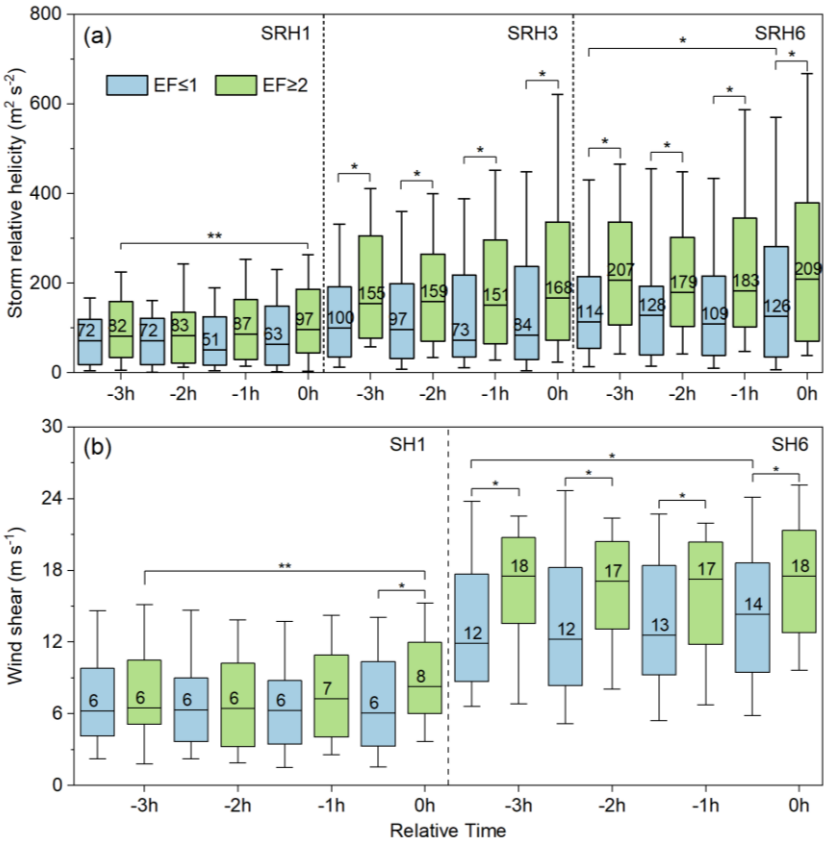

Figure 8. As in Figure 7, but for kinematic parameters: (a) storm-relative helicity and (b) vertical wind shear.

Figure 8a illustrates the temporal evolution of SRH across three altitude layers within significant and weak tornadic environments. A distinct feature is that, across all evaluated time steps (from -3 h to 0 h), the median SRH values for significant tornadoes (EF ≥ 2) surpass those for weak tornadoes (EF ≤ 1) at all three vertical levels. The magnitude of the SRH discrepancy between the two intensity groups expands with increasing height. This expanding vertical gradient signifies that significant tornadogenesis requires not only stronger low-level rotation but also mid-to-upper-level deep kinematic forcing (i.e., SRH3 and SRH6).

The two tornado categories exhibit distinct pre-storm evolution. As indicated by the significance markers in the figure, SRH1, SRH3, and SRH6 for significant tornadoes all exhibit statistically significant, continuous ascending trends (Friedman test, $p < 0.01$, $p < 0.05$, $p < 0.05$, respectively). None of the SRH layers for weak tornadoes demonstrate any statistically significant pre-storm amplification. A closer examination of the actual median evolution immediately prior to initiation (from -2 h to 0 h) reveals that significant tornadoes achieve substantial helicity accumulation across all layers. SRH6 increases by 30 $m^2 s^{-2}$ (leaping from 179 to 209). However, weak tornadoes not only fail to intensify but exhibit stagnation or even marginal decay (with increments across all layers falling below zero). In summary, the occurrence of significant tornadoes demands not only a superior overall baseline SRH environment but is accompanied by a substantial, abrupt amplification and accumulation of deep-layer kinematics (SRH6) shortly before tornadogenesis. This rapid kinematic buildup constitutes a critical dynamic signature for differentiating the potential of significant versus weak tornadoes.

Figure 8b compares the temporal evolution of low-level (SH1) and deep-layer (SH6) SH between the two intensity groups. Consistent with the stronger SRH observed in significant tornadoes, their median SH values across both layers consistently equal or exceed those of weak tornadoes at all time steps. Particularly at the exact time of tornadogenesis (0 h), the median SH1 and SH6 for significant tornadoes (8 m s^{-1} and 18 m s^{-1}, respectively) are distinctly stronger than their weak counterparts (6 m s^{-1} and 14 m s^{-1}, respectively).

 doi:10.20944/preprints202604.0756.v1

Rigorous statistical testing clarifies the underlying trends despite the overlapping distributions in the box plots. SH1 for significant tornadoes undergoes a highly significant intensifying process prior to genesis ($p < 0.01$, with the median escalating from 6 to 8 m s^{-1}). Simultaneously, SH6 for both tornado categories also exhibits a degree of statistically significant temporal evolution ($p < 0.05$). Based on the aforementioned kinematic and thermodynamic analyses, the typical environment conducive to significant tornadoes (EF ≥ 2) not only possesses a large amount of MLCAPE but is also modulated by intense mid-to-upper-level deep kinematic conditions. Specifically, intense SRH6 and SH6 play a decisive and governing role in dictating the ultimate intensity of the tornado.

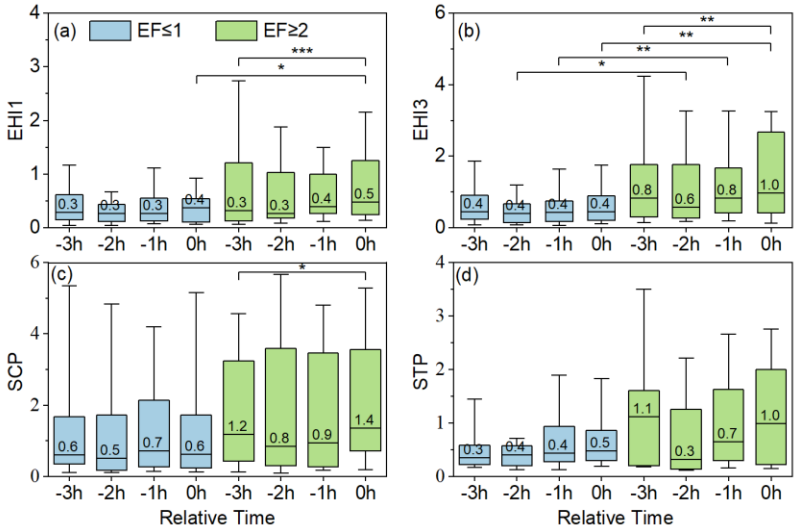

Figure 9. As in Figure 7, but for composite parameters: (a) EHI1, (b) EHI3, (c) SCP, and (d) STP.

Tornado intensity is driven by complex interactions between deep-layer thermodynamic and kinematic environmental factors. Individual parameters are often insufficient to comprehensively depict this complex tornadogenesis potential. To address this, Figure 9 further illustrates the spatiotemporal evolutionary relationships between composite parameters and tornado intensity. In contrast to the complex regional patterns observed in the north-south stratification (Figure 4), the median values of all composite parameters for significant tornadic environments (EF ≥ 2) exceed those for weak tornadoes (EF ≤ 1). Moreover, this elevated baseline is accompanied by a much more pronounced, abrupt pre-storm amplification of specific parameters immediately prior to tornadogenesis.

EHI within significant tornadic environments exhibits a clear precursor signature (Figure 9a and 9b). The low-level EHI1 shows a statistically highly significant, continuous surging trend prior to genesis (Friedman test, $p < 0.001$). Simultaneously, the mid-to-upper-level EHI3 not only remains significantly stronger than that of weak tornadoes across all evaluated time steps (Mann-Whitney U test, $p < 0.05$ or 0.01), but also undergoes a rapid pre-storm amplification ($p < 0.01$). At exactly 0 h, its median attains 1.0, aligning with the classical operational warning threshold (EHI > 1.0) indicative of environments conducive to significant tornadogenesis [8]. Regarding SCP (Figure 9c), significant tornadoes not only possess a superior background baseline (achieving a median of 1.4 at 0 h, far surpassing the 0.6 observed for weak tornadoes), but rigorous statistical testing also reveals that its temporal trajectory is by no means static. Instead, it experiences a statistically significant fluctuating evolution ($p < 0.05$, characterized by an initial decline followed by a subsequent ascent).

STP (Figure 9d) likewise exhibits a prominent numerical difference between the two intensity groups. On the one hand, at 0 h, the median STP for significant tornadoes (1.0) is double that of weak tornadoes (0.5). Although STP exhibits numerical fluctuations, these variations do not pass the Friedman significance test ($p > 0.05$), indicating substantial inter-event variability. Therefore, the short-term temporal evolution of STP may not serve as a universal precursor.

 doi:10.20944/preprints202604.0756.v1

In summary, the occurrence of significant tornadoes relies not only on a favorable initial background baseline of composite parameters, but is also accompanied by pronounced, short-term pre-storm increases in these key indices (particularly EHI), culminating in the definitive breach of critical thresholds (e.g., 1.0) at 0 h. These dynamic evolutionary signatures, captured by high-frequency satellite observations, provide valuable, quantitative precursor signals for the operational short-term nowcasting and warning of significant tornadoes.

4. Conclusions and Discussion

Based on the joint application of high-frequency Himawari-8 satellite TBB observations and ERA5 reanalysis, this study tracked the pre-tornadic convective centers of 177 tornadoes in China, mitigating the spatial blind spots inherent in radar networks. The spatiotemporal evolution of near-storm environments was analyzed, yielding the following main conclusions:

(1) Difference of Regional Environmental Paradigms: Tornadogenesis in China follows two distinctly divergent regional mechanisms. Southern tornadoes are "dynamically driven," occurring in humid conditions with minimal CIN and low MLLCL (median: 790 m). Their genesis is dominated by strong low-level kinematics (SH1 and SRH1). In contrast, northern tornadoes follow a "coupled thermodynamic-kinematic" paradigm. Governed by deep cold vortices, they occur in drier environments with higher CIN (median: 30 J kg^{-1}), acting as a natural filter. Their triggering relies on the rapid, concurrent amplification of MLCAPE (increasing by ~211 J kg^{-1} within 3 hours) and deep-layer kinematics (SRH6 and SH6) shortly before tornadogenesis.

(2) Environmental Precursors for Significant Tornadoes: Significant tornadoes (EF ≥ 2) occur in superior parameter spaces compared to weak tornadoes (EF ≤ 1). Thermodynamically, strong tornadoes possess much higher MLCAPE (median: 902 vs. 677 J kg^{-1}) and feature a unique pre-storm boundary layer moistening process, evidenced by a noticeable drop in MLLCL coupled with rapidly cooling cloud tops captured by satellite (TBB ≤ -73 °C). Kinematically, they require stronger deep-layer shear (SH6 median: 18 m s^{-1}) and deep-layer helicity (SRH6 median: 209 m^2 s^{-2}).

(3) Nowcasting Value of Satellite Data and Composite Parameters: The temporal rate of change serves as a critical predictor. The continuous pre-storm rapid cooling of Himawari-8 TBB captures the rapid vertical expansion of parent updrafts.

Although statistical results derived from large-scale environmental parameters cannot replace high-frequency radar observations as absolute, standalone warning thresholds for tornadogenesis, they offer novel quantitative insights into the climatological characteristics and regional disparities of tornadoes in China. They offer a physical explanation for the higher proportion of significant tornadoes observed in northern China. This study posits that this phenomenon is associated with the typical northern environmental background. On the one hand, elevated MLCIN filters out weak, premature convection. This suppression acts as an "energy lid" (or capping inversion), fostering the requisite conditions for the rapid accumulation of instability and ensuring that severe convection is triggered within a substantially more energetic environment. On the other hand, this phenomenon is associated with the fact that northern tornadogenesis is dependent on much more deep-layer kinematic forcing (i.e., significantly larger magnitudes of deep-layer SRH3 and SRH6). This hypothesis requires further validation using detailed case studies and high-resolution vertical moisture profiles. Future work should explore the physical mechanisms driving the distinct vertical distributions of kinematic parameters (e.g., SRH) between northern and southern China.

This study possesses certain limitations. The primary limitation of this study is the sample size. Restricted by the currently available volume of reliably documented events, this research stratified the tornadoes into broad northern and southern cohorts, precluding more granular categorizations based on specific synoptic backgrounds or finer geographical sub-regions (particularly when separately comparing significant and weak tornadoes). In reality, as illustrated in Figure 1, tornadic occurrences in China are concentrated in three predominant high-frequency zones: Northeast China, the Jianghuai region (centered around northern Jiangsu Province), and the southern coastal region (centered around Guangdong Province). The tornado climatology across these three sub-regions

 doi:10.20944/preprints202604.0756.v1

possesses objective discrepancies. However, future studies will benefit from the Key Laboratory for Tornadoes, CMA, established in 2023. The database will alleviate current sample size limitations, providing support for conducting more refined, sub-regional climatological investigations in the future.

Secondly, the spatiotemporal resolution of the ERA5 reanalysis data (0.25°, 1 h) relied upon herein exhibits a scale mismatch when compared to the authentic microscale characteristics of tornadic parent storms. This disparity likely leads to an unavoidable underestimation of the extreme parameter peaks localized within the storm's intense convective core. Currently, high-frequency soundings and targeted observations of Chinese tornadoes remain scarce. By analyzing the spatiotemporal evolution of near-storm environments, this study provides important directions for future fine-scale storm observations. Furthermore, it establishes a quantitative baseline for extracting and verifying warning indices from extensive Doppler radar datasets.

Author Contributions: Conceptualization, Y.Z.; methodology, Y.Z.; software, C.C., Y.C. and R.L.; val-idation, Y.Z. and R.L.; formal analysis, Y.Z., C.C. and R.L.; investigation, C.C., and Y.C.; resources, Y.Z. and X.K.; data curation, C.C. and Y.C.; writing—original draft preparation, Y.Z. and C.C.; writing—review and editing, Y.Z., K.Z. and R.L.; visualization, C.C., Y.Z. and Y.C.; supervision, Y.Z., Y.L. and Q.Z.; project administration, Y.Z. and X.K.; funding acquisition, Y.Z. and X.K. All authors have read and agreed to the published version of the manuscript.

Funding: This research was funded by the Second Tibetan Plateau Scientific Expedition and Re-search (STEP) Program (Grant No. 2019QZKK0104) and the National Natural Science Foundation of China (Grant No. 41875002).

Data Availability Statement: The tornado event data utilized in this study are derived from published climatological reports and the Tornado Database in China (2017–2020), which is publicly archived on the Peking University Open Research Data Platform at https://opendata.pku.edu.cn/dataset.xhtml?persistentId=doi:10.18170/DVN/M7PTV9. The Himawari-8 TBB data can be accessed through the Japan Meteorological Agency (JMA) at https://www.jma.go.jp/jma/jma-eng/satellite/dissemination.html. The global ERA5 reanalysis data are provided by the European Centre for Medium-Range Weather Forecasts (ECMWF) Copernicus Climate Change Service (C3S) and can be accessed at https://cds.climate.copernicus.eu/. The processed data and analysis codes generated during this study are available from the corresponding author upon reasonable request.

Acknowledgments: We acknowledge the Copernicus Climate Change Service (C3S) Climate Data Store (CDS) for providing the ERA5 reanalysis data. We also thank the Japan Meteorological Agency (JMA) for providing the Himawari-8 satellite data. We are grateful to the local meteorological departments and the Key Laboratory for Tornadoes, China Meteorological Administration (CMA), for their support in the cross-verification of tornado records. Finally, the authors thank the anonymous reviewers and editors for their constructive comments, which greatly improved the quality of this manuscript.

Conflicts of Interest: The authors declare no conflicts of interest.

Abbreviations

The following abbreviations are used in this manuscript:

TBB	Cloud-top brightness temperature

 doi:10.20944/preprints202604.0756.v1

LCL	Lifted Condensation Level
CIN	Convective Inhibition
SRH	Storm-relative helicity
SRH1	SRH within the 0–1 km layers
SRH3	SRH within the 0–3 km layers
SRH6	SRH within the 0–6 km layers
CAPE	Convective available potential energy
MLCAPE	Mixed-Layer convective available potential energy
EF	Enhanced Fujita scale
EHI	Energy-Helicity Index
STP	Significant Tornado Parameter
SH	Vertical wind shear
SH1	SH within the 0–1 km layers
SH3	SH within the 0–3 km layers
SH6	SH within the 0–6 km layers
SCP	Supercell Composite Parameter
HSLC	High-shear, low-CAPE
CMA	China Meteorological Administration
S. China	Southern China group
N. China	Northern China group
MLCIN	Mixed-Layer Convective Inhibition
TC	Tropical cyclone
KDE	Bivariate kernel density estimation
WNPSH	the western North Pacific subtropical high
LLJ	Low-level jet

Appendix A

 doi:10.20944/preprints202604.0756.v1

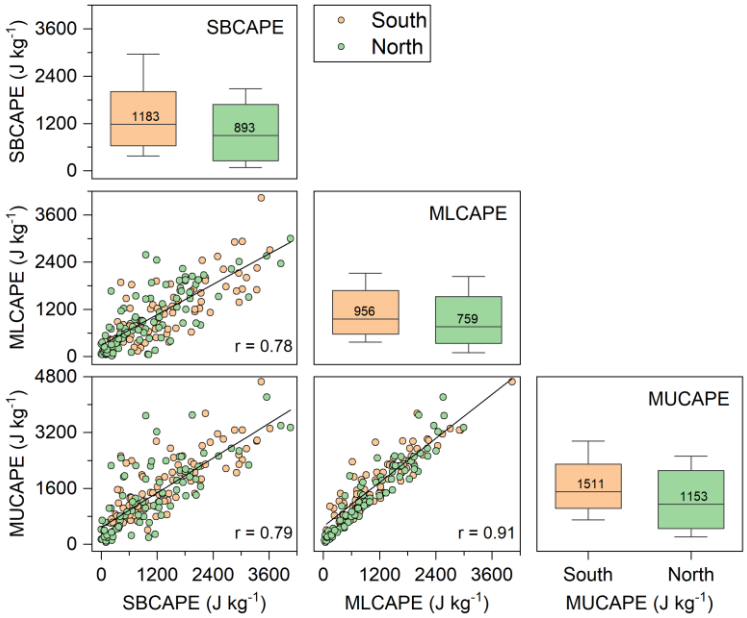

Figure A1. Combined scatter plots of the three types of CAPE for 177 tornado events. (The box lines are the 10th, 25th, 50th, 75th, and 90th percentiles from the bottom to the top.)

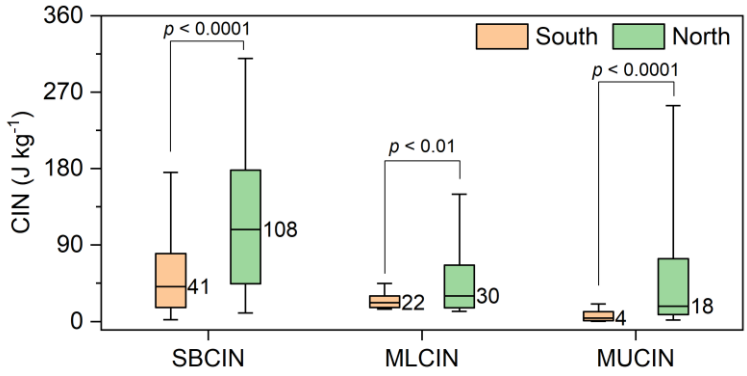

Figure A2. Comparison of the three types of CIN in 177 tornadoes.

Appendix B

 doi:10.20944/preprints202604.0756.v1

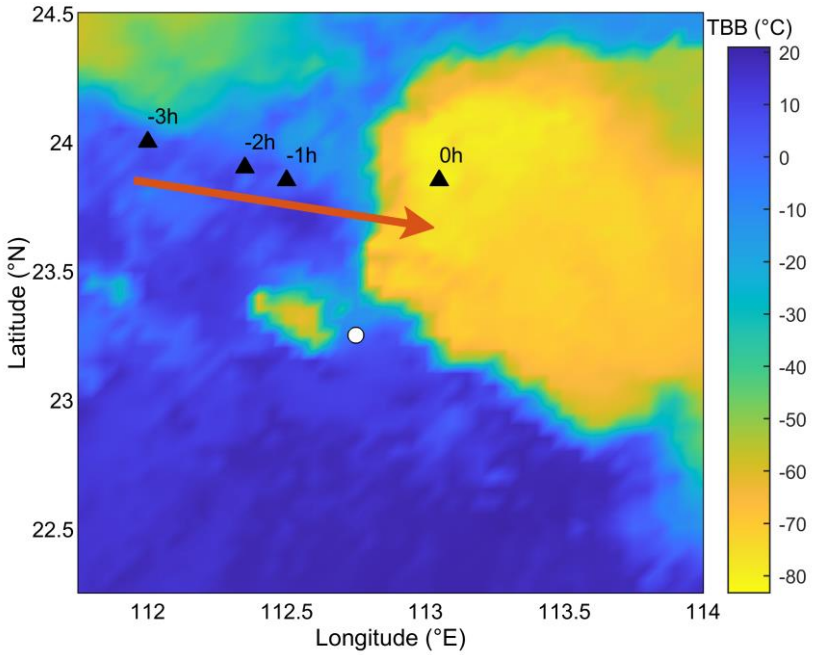

Figure A3. Localization of the convective center associated with a tornado based on TBB, where ○ is the location of tornado occurrence and ▲ are the locations of the thunderstorm cloud TBB minima. (Using the example of the Foshan EF3 tornado at 17:00 on 9 May 2016).

References

1. Chen, J.; Cai, X.; Wang, H.; Kang, L.; Zhang, H.; Song, Y.; Zhu, H.; Zheng, W.; Li, F. Tornado climatology of China. *Int. J. Climatol.* **2018**, *38*, 2478-2489. https://doi.org/10.1002/joc.5369.
2. Zhu, W.; Sheng, J.; Zheng, Y.; Yang, B.; Zhang, X.; Fan, L.; Zhang, X.; Liu, X.; Cao, Y.; Lin, Y.; et al. Damage survey and mesoscale features analysis on tornado in outer rain-band of typhoon "Mujigae" on 4 October 2015. *Torrential Rain Disasters* **2016**, *35*, 403-414. https://doi.org/10.3969/j.issn.1004-9045.2016.05.002. (In Chinese)
3. Zhi, J.; Huang, X.; Bai, L.; Cai, K.; Li, C.; Li, Z.; Zhang, J.; Guan, L.; Sheng, J.; Zhou, K.; et al. Characteristics of Tornado Activity and Disaster of China in 2021. *Adv. Meteorol. Sci. Technol.* **2022**, *12*, 23-36. https://doi.org/10.3969/j.issn.2095-1973.2022.01.004shu. (In Chinese)
4. Yu, X.; Zhao, J.; Fan, W. Tornadoes in China: Spatiotemporal Distribution and Environmental Characteristics. *J. Trop. Meteorol.* **2021**, *37*, 681-692. https://doi.org/10.16032/j.issn.1004-4965.2021.064. (In Chinese)
5. Anderson-Frey, A.K.; Richardson, Y.P.; Dean, A.R.; Thompson, R.L.; Smith, B.T. Characteristics of Tornado Events and Warnings in the Southeastern United States. *Weather Forecasting* **2019**, *34*, 1017-1034. https://doi.org/10.1175/waf-d-18-0211.1.
6. Brooks, H.E.; Lee, J.W.; Craven, J.P. The spatial distribution of severe thunderstorm and tornado environments from global reanalysis data. *Atmos. Res.* **2003**, *67-68*, 73-94. https://doi.org/10.1016/s0169-8095(03)00045-0.
7. Sherburn, K.D.; Parker, M.D. Climatology and ingredients of significant severe convection in high-shear, low-CAPE environments. *Weather Forecasting* **2014**, *29*, 854-877. https://doi.org/10.1175/WAF-D-13-00041.1.
8. Thompson, R.L.; Edwards, R.; Hart, J.A.; Elmore, K.L.; Markowski, P. Close proximity soundings within supercell environments obtained from the Rapid Update Cycle. *Weather Forecasting* **2003**, *18*, 1243-1261. https://doi.org/10.1175/1520-0434(2003)018<1243:CPSWSE>2.0.CO;2.
9. Thompson, R.L.; Smith, B.T.; Dean, A.R.; Marsh, P.T. Spatial distributions of tornadic near-storm environments by convective mode. *E-J. Severe Storm Meteorol.* **2013**, *8*, 1-22. https://doi.org/10.55599/ejssm.v8i5.50.

 doi:10.20944/preprints202604.0756.v1

10. Coffer, B.E.; Parker, M.D.; Thompson, R.L.; Smith, B.T.; Jewell, R.E. Using Near-Ground Storm Relative Helicity in Supercell Tornado Forecasting. *Weather Forecasting* **2019**, *34*, 1417-1435. https://doi.org/10.1175/waf-d-19-0115.1.
11. Davies-Jones, R. Streamwise Vorticity: The Origin of Updraft Rotation in Supercell Storms. *J. Atmos. Sci.* **1984**, *41*, 2991-3006. https://doi.org/10.1175/1520-0469(1984)041<2991:SVTOOU>2.0.CO;2.
12. Qie, X.; Qie, K.; Wei, L.; Zhu, K.; Sun, Z.; Yuan, S.; Jiang, R.; Zhang, H.; Xu, C. Significantly Increased Lightning Activity Over the Tibetan Plateau and Its Relation to Thunderstorm Genesis. *Geophys. Res. Lett.* **2022**, *49*. https://doi.org/10.1029/2022gl099894.
13. Qie, X.; Toumi, R.; Yuan, T. Lightning activities on the Tibetan Plateau as observed by the lightning imaging sensor. *J. Geophys. Res. Atmos.* **2003**, *108*. https://doi.org/10.1029/2002jd003304.
14. Weisman, M.L.; Klemp, J.B. The dependence of numerically simulated convective storms on vertical wind shear and buoyancy. *Mon. Weather Rev.* **1982**, *110*, 504-520. https://doi.org/10.1175/1520-0493(1982)110<0504:TDONSC>2.0.CO;2.
15. Rasmussen, E.N. Refined supercell and tornado forecast parameters. *Weather Forecasting* **2003**, *18*, 530-535. https://doi.org/10.1175/1520-0434(2003)18<530:RSATFP>2.0.CO;2.
16. Rasmussen, E.N.; Blanchard, D.O. A baseline climatology of sounding-derived supercell andtornado forecast parameters. *Weather Forecasting* **1998**, *13*, 1148-1164. https://doi.org/10.1175/1520-0434(1998)013<1148:ABCOSD>2.0.CO;2.
17. Anderson-Frey, A.K.; Richardson, Y.P.; Dean, A.R.; Thompson, R.L.; Smith, B.T. Investigation of Near-Storm Environments for Tornado Events and Warnings. *Weather Forecasting* **2016**, *31*, 1771-1790. https://doi.org/10.1175/waf-d-16-0046.1.
18. Taszarek, M.; Pilguj, N.; Allen, J.T.; Gensini, V.; Brooks, H.E.; Szuster, P. Comparison of convective parameters derived from ERA5 and MERRA-2 with rawinsonde data over Europe and North America. *J. Clim.* **2021**, *34*, 3211-3237. https://doi.org/10.1175/JCLI-D-20-0484.1.
19. Zheng, Y. Review of Climatology and Favorable Environmental Conditions of Tornado in China. *Adv. Meteorol. Sci. Technol.* **2020**, *10*, 67-75. https://doi.org/10.3969/j.issn.2095-1973.2020.06.012. (In Chinese)
20. Huang, X.; Bai, L.; Yan, L.; Zhang, Z.; Cai, K.; Zhi, J. Climatic characteristics and environmental conditions of the tornado occurrences within tropical cyclones over Guangdong province, China. *Acta Meteorol. Sin.* **2024**. https://doi.org/10.11676/qxxb2024.20230125. (In Chinese)
21. Wang, L.; Wang, X.; Li, Y.; Zhang, J.; Wang, Y.; Lyu, R. Multi-Scale Characteristic Analysis and Warning Thoughts of EF2 Tornado in Gaoyou County, Jiangsu Province in 2020. *Meteorol. Mon.* **2023**, *49*, 291-303. https://doi.org/10.7519/j.issn.1000-0526.2022.071801. (In Chinese)
22. Cai, K.; Yao, X.; Sun, X.; Cheng, P. Climatic characteristics and environmental conditions of tornadoes in Liaoning under the background of cold vortex. *Acta Meteorol. Sin.* **2022**, 82-92. https://doi.org/10.11676/qxxb2021.063. (In Chinese)
23. Yuan, C.; Yang, W.; Li, D.; Yang, L.; Wang, S. Climatology and Environmental Feaures of Tornadoes in Liaoning Province During 1971-2020. *Meteorol. Mon.* **2023**, *49*, 1285-1298. https://doi.org/10.7519/j.issn.1000-0526.2023.032601. (In Chinese)
24. Cai, K.; Huang, X.; Li, C.; Yan, L.; Li, Z.; Gu, B.; He, Q.; Zhang, J. Characteristics of Tornado Activity in China in 2020. *Adv. Meteorol. Sci. Technol.* **2021**, *11*, 40–45, 53. https://doi.org/10.3969/j.issn.2095-1973.2021.01.007. (In Chinese)
25. Huang, S.; Li, Z.; Bai, L.; Huang, X.; Zhi, J.; Xu, Z.; Liu, Y. Characteristics of Tornado Activity and Related Disasters in China in 2022. *Adv. Meteorol. Sci. Technol.* **2023**, *13*, 23-32. https://doi.org/10.3969/j.issn.2095-1973.2023.01.004. (In Chinese)
26. Huang, X.; Yan, L.; Cai, K.; Li, Z. Characteristics of Tornado Activity in China in 2018. *Adv. Meteorol. Sci. Technol.* **2019**, *9*, 50-55. https://doi.org/10.3969/j.issn.2095-1973.2019.01.009. (In Chinese)
27. Li, C.; Tan, H.; Cai, K.; Bai, L.; Huang, X.; Yan, L.; Li, Z.; Zhi, J.; Zhang, J. Characteristics of Tornado Activity in China in 2019. *Adv. Meteorol. Sci. Technol.* **2020**, *10*, 7-14. https://doi.org/10.3969/j.issn.2095-1973.2020.01.003. (In Chinese)

 doi:10.20944/preprints202604.0756.v1

28. Li, C.; Tan, H.; Cai, K.; Bai, L.; Huang, X.; Yan, L.; Li, Z.; Zhi, J.; Zhang, J. Tornadoes in China and Their Disaster Characteristics from 2016 to 2020. *J. Trop. Meteorol.* **2021**, *37*, 733-747. https://doi.org/10.16032/j.issn.1004-4965.2021.068. (In Chinese)
29. Zhang, J.; Huang, X.; Cai, K.; Zhi, J.; Huang, S.; Xu, Z. Tornado Activities and Disaster Characteristics in China in 2023. *Adv. Meteorol. Sci. Technol.* **2024**, *14*, 15-24. https://doi.org/10.3969/j.issn.2095-1973.2024.01.003. (In Chinese)
30. Zhou, R.; Meng, Z. Tornado Database in China (2017~2020). Peking University Open Research Data Platform, V1. **2023**. https://doi.org/10.18170/DVN/M7PTV9.
31. Du, Y.; Zheng, D.; Ma, R.; Zhang, Y.; Lyu, W.; Yao, W.; Zhang, W.; Ciren, L.; Cuomu, D. Thunderstorm Activity over the Qinghai–Tibet Plateau Indicated by the Combined Data of the FY-2E Geostationary Satellite and WWLLN. *Remote Sens.* **2022**, *14*, 2855. https://doi.org/10.3390/rs14122855.
32. Doswell, C.A.; Brooks, H.E.; Dotzek, N. On the implementation of the enhanced Fujita scale in the USA. *Atmos. Res.* **2009**, *93*, 554-563. https://doi.org/10.1016/j.atmosres.2008.11.003.
33. Zhang, C.; Xue, M.; Zhu, K.; Yu, X. Climatology of significant tornadoes within China and comparison of tornado environments between the United States and China. *Mon. Weather Rev.* **2023**, *151*, 465-484. https://doi.org/10.1175/MWR-D-22-0070.1.
34. Bessho, K.; Date, K.; Hayashi, M.; Ikeda, A.; Imai, T.; Inoue, H.; Kumagai, Y.; Miyakawa, T.; Murata, H.; Ohno, T. An introduction to Himawari-8/9—Japan's new-generation geostationary meteorological satellites. *J. Meteorol. Soc. Jpn. Ser. II* **2016**, *94*, 151-183. https://doi.org/10.2151/jmsj.2016-009.
35. Hersbach, H.; Bell, B.; Berrisford, P.; Hirahara, S.; Horányi, A.; Muñoz-Sabater, J.; Nicolas, J.; Peubey, C.; Radu, R.; Schepers, D.; et al. The ERA5 global reanalysis. *Q. J. R. Meteorol. Soc.* **2020**, *146*, 1999-2049. https://doi.org/10.1002/qj.3803.
36. Markowski, P.; Richardson, Y. *Mesoscale meteorology in midlatitudes*; John Wiley & Sons: 2011.
37. Romps, D.M. Exact expression for the lifting condensation level. *J. Atmos. Sci.* **2017**, *74*, 3891-3900. https://doi.org/10.1175/JAS-D-17-0102.1.
38. Zhao, Y.; Bi, L.; Kong, X. Identification and feature analysis of thunderstorm based on AGRI and LMI of Fengyun-4A satellite. *Atmos. Res.* **2025**, *318*, 108016. https://doi.org/10.1016/j.atmosres.2025.108016.
39. Qie, X.; Wu, X.; Yuan, T.; Bian, J.; Lu, D. Comprehensive Pattern of Deep Convective Systems over the Tibetan Plateau–South Asian Monsoon Region Based on TRMM Data. *J. Clim.* **2014**, *27*, 6612-6626. https://doi.org/10.1175/JCLI-D-14-00076.1.
40. Markowski, P.M.; Richardson, Y.P. The Influence of Environmental Low-Level Shear and Cold Pools on Tornadogenesis: Insights from Idealized Simulations. *J. Atmos. Sci.* **2014**, *71*, 243-275. https://doi.org/10.1175/jas-d-13-0159.1.